Long-term Stable 2*D* Dion-Jacobson Phase Perovskite Photodiode with Low Dark Current and High On/off Ratio①

GU Hao[a, b] CHEN Shan-Ci[b②] ZHENG Qing-Dong[b②]

[a] (*College of Chemistry, Fuzhou University, Fuzhou* 350000, *China*)

[b] (*State Key Laboratory of Structural Chemistry, Fujian Institute of Research on the Structure of Matter, Chinese Academy of Sciences, Fuzhou* 350002, *China*)

ABSTRACT A two-dimensional (2*D*) organic-inorganic hybrid perovskite (OIHP) material is considered as a promising candidate for a long-term stable photodetector owing to its outstanding phase and environmental stability. Herein, we demonstrate a perovskite photodiode based on the DJ phase 2*D* perovskite (PDA)$(MA)_{n-1}Pb_nI_{3n+1}$ (where PDA is 1,3-propylenediamine, MA is methylamine, nominal n = 4). The best-performance device exhibits a high detectivity of 4.57×10^{11} Jones, a responsivity of 0.25 $A \cdot W^{-1}$ at 480 nm, a low dark current density of 9.60×10^{-4} $mA \cdot cm^{-2}$, and a remarkable on/off ratio of 3.10×10^5. The unencapsulated device can maintain 95% of the initial photocurrent density after 90 days under an ambient atmosphere with relative humidity (RH) of 65%, demonstrating its improved stability than the 3*D* counterpart. The excellent stability of the photodiode based on 2*D* perovskite promises its bright commercial application future.

Keywords: two-dimensional perovskite, Dion-Jacobson, photodiode, on/off ratio, stability;

DOI: 10.14102/j.cnki.0254-5861.2011-3200

1 INTRODUCTION

As a kind of photoelectronic devices to convert optical signals into electrical signals, photodetectors are widely used in aerospace communication, environmental monitor, biological sensor, and other fields[1-5]. At present, commercial photodetectors are mostly based on III-V inorganic semiconductors such as silicon (Si) and germanium (Ge), but they have the drawbacks of high cost and complicated fabrication process[6-9]. Therefore, it is urgent to fabricate photodetectors with low cost and simple preparation process. In recent years, perovskite materials have attracted increasing attention due to their excellent merits including high carrier mobility, adjustable bandgap, long charge diffusion length, and simple fabrication process[10-13]. As a typical organic-inorganic hybrid perovskite (OIHP), $CH_3NH_3PbI_3$ ($MAPbI_3$) has been used for various practical applications such as solar cells, light-emitting diodes (LED), photodetectors, lasers, etc.[14-18]. However, the poor moisture and heat stability is still a problem that needs to be solved. Recently, two-dimensional (2*D*) OIHP materials, which are fabricated by adding a long chain or large volume organic ammonium salt to the perovskite components[19, 20], are emerging due to their great potential to solve the stability issue of the conventional three-dimensional (3*D*) perovskite materials.

The 2*D* OIHP material was first used to improve the performance of solar cells. Smith et al. used $(PEA)_2(MA)_2Pb_3I_{10}$ (where PEA^+ is phenylethylammonium) as the active layer to fabricate solar cells with improved stability[21]. Some other organic ammonium salts have also been used to prepare 2*D* OIHP, such as 1,3-propylenedia- mine (PDA)[19], butylamine (BA)[22], and so on. The encouraging results of solar cells based on 2*D* perovskites inspire researchers to further explore other applications of the 2*D* perovskites. For example, Han et al. fabricated highly oriented thin films with a new 2*D* perovskite $(PA)_2(FA)Pb_2I_7$ (where PA is *n*-pentylaminium and FA is formamidine) for photodetectors,

Received 31 March 2021; accepted 26 May 2021

① Supported by the National Natural Science Foundation of China (No. U1605241), the Fujian Science & Technology Innovation Laboratory for Optoelectronic Information of China (No. 2021ZR116) and the Natural Science Foundation of Fujian Province for Distinguished Young Scholars (No. 2019J06023)

② Corresponding authors. E-mails: scchen@fjirsm.ac.cn and qingdongzheng@fjirsm.ac.cn

which realized an ultrafast response time of 2.54 ns as well as a high responsivity of 1.73×10^{14} Jones[23]. Tsai et al. used a 2*D* perovskite $(BA)_2(MA)_2Pb_3I_{10}$ for X-ray photodiodes that can work at a very low external bias[24]. Lim et al. developed a photodiode based on 2*D* perovskite by incorporating PEAI into $MAPbI_3$. The current density of the 2*D* perovskite photodiode maintained 76% of the initial current density after 80 days in the ambient condition, compared to 15% for the control sample of 3*D* perovskite photodiode[25].

According to the types of organic amines used in the 2*D* perovskite, 2*D* perovskite can be divided into Ruddlesden-Popper (RP) and Dion-Jacobson (DJ) phases, which are prepared by using monoamine and diamine, respectively[26]. The RP phase 2*D* perovskite has a general formula of $(RNH_3)_2A_{n-1}M_nX_{3n+1}$, in which the monoammonium cations only interact with inorganic perovskite layers at one side, and van der Waals gap exists between the adjacent cations. In the DJ phase 2*D* perovskite with a formula of $(NH_3RNH_3)A_{n-1}M_nX_{3n+1}$, hydrogen bonds are formed between the amino group and the inorganic component at both ends. Compared with the RP phase 2*D* perovskites, the DJ ones can possess better stability owing to the elimination of the van der Waals gap (see illustration in Fig. 1)[19, 27]. So far, there are only a few reports about the DJ phase perovskites for photodetectors[28, 29]. And, in the reports, a photoconductor device configuration was adopted for the DJ phase 2*D* perovskite photodetectors, which usually needs relatively high operating voltages. Meanwhile, they suffer from low on/off ratios ($< 10^3$) which limit their further applications. In contrast, photodiode-type photodetectors can work at zero bias and exhibit high on/off ratios owing to the rather low dark currents although their EQEs are normally less than 1. To the best of our knowledge, DJ phase 2*D* perovskites have never been used for fabricating the photodiode-type photodetectors until now.

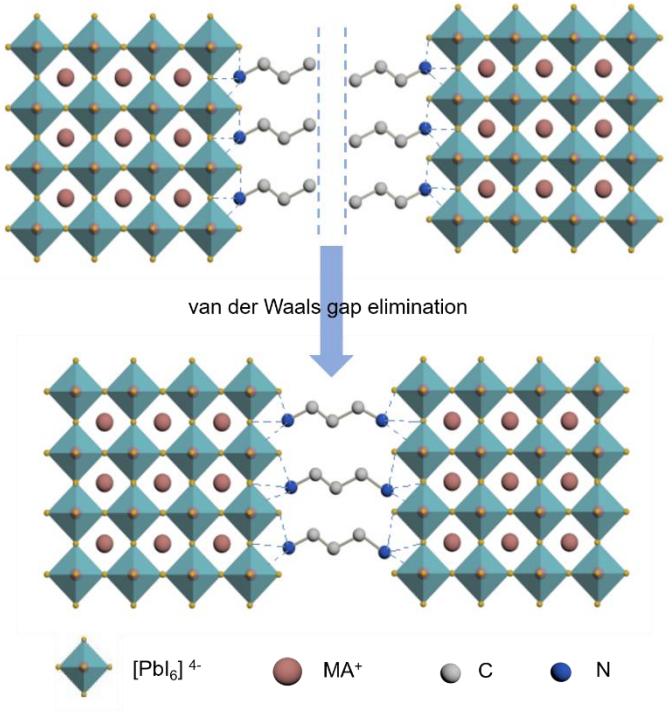

Fig. 1. Schematic illustration of RP and DJ phase 2*D* perovskites

Herein, we fabricated a high-performance stable photodetector based on a DJ phase 2*D* perovskite derived from 1,3-propyleneamine (PDA). A high-quality film of $(PDA)(MA)_{n-1}Pb_nI_{3n+1}$ (nominal $n = 4$) was prepared by one-step method. The resulting photodiodes exhibit lower dark current and better stability than the 3*D* reference devices. The device based on DJ phase 2*D* perovskite exhibits a responsivity of 0.25 $A \cdot W^{-1}$ and a high detectivity of 4.57×10^{11} Jones at 480 nm. In addition, the device has a dark current density as low as 9.60×10^{-4} $mA \cdot cm^{-2}$ and a maximum on/off ratio of 3.10×10^5, which are remarkable in the 2*D* perovskite photodiodes. Furthermore, the devices based on the DJ phase 2*D* perovskite layer without encapsulation can maintain 95% of the initial photocurrent

after storage for 90 days in the air with a relative humidity (RH) of 65%, while the conventional 3*D* perovskite photodiodes can only maintain 35% of the initial photocurrent after the same storage time.

2 EXPERIMENTAL

2. 1 Materials

1,3-Propylenediamine and hydroiodic acid were purchased from Aladdin. The SnO_2 colloid precursor (Tin (IV) oxide, 15% in H_2O colloidal dispersion) was purchased from Alfa Aesar. Lead iodide (PbI_2) and methylammonium iodide (MAI) were purchased from Xi'an Polymer Technology Crop..Dimethylformamide (DMF), dimethylsulfoxide (DMSO), *γ*-butyrolactone (GBL), and chlorobenzene (CB) were purchased from Sigma-Aldrich. 2,2′,7,7′-Tetrakis[*N*,*N*-di(4-methoxyphenyl)amino]-9,9′-spirobifluorene (Spiro-OMeTAD) was purchased from Shenzhen Feiming Science and Technology Co., Ltd.

2. 2 Synthesis of $(PDA)I_2$

1,3-Propylenediamine iodide ($(PDA)I_2$) was prepared by adding dropwise hydroiodic acid (3.40 mL, 30 mmol) to a solution of 1,3-propylenediamine (0.74 g, 10 mmol) in ethanol at 0 ℃ and stirring for 2 h[19]. The white precipitate of the diammonium iodide was recovered by evaporating the solvent at 55 ℃ using a rotary evaporator. The precipitate was washed three times with ether and dried overnight in an oven at 60 ℃ under reduced pressure to obtain a white powder (1.70 g, 85% yield).

2. 3 Preparation of 2*D* perovskite film

The 2*D* perovskite $PDA(MA)_3Pb_4I_{13}$ precursor solutions (the concentration of Pb^{2+} is 0.8 M) were prepared by dissolving a stoichiometric ratio of 4:3:1 of PbI_2, MAI, and $(PDA)I_2$ in the mixed solution of GBL:DMSO (7:3, volume ratio), and then stirred at 65 ℃ before use. The prepared solutions were filtered by PTFE syringe filter (0.2 μm) and coated onto the substrate with a consecutive spin-coating process at 6000 rpm for 35 s. Before the end of 15 s, 100 μL of chlorobenzene was dropped onto the perovskite film for better crystallization, followed by annealing at 120 ℃ for 10 min.

2. 4 Fabrication of devices

ITO glass substrates were cleaned *via* sequential ultrasonic treatments with acetone, isopropyl alcohol, and deionized water for 30 min, respectively. Then, they are dried in the oven at 75 ℃. Before deposition of the SnO_2 electron transport layer (ETL), the ITO substrates were pretreated by UV-O_3 for 15 min. And the SnO_2 colloid solution with a concentration of 7.5 wt% was spin-coated on the ITO at 3000 rpm for 30 s, followed by annealing at 120 ℃ for 10 min and 150 ℃ for 20 min. Then, the coated substrates were transferred to a N_2-filled glovebox to deposit the perovskite onto the ETL using the aforementioned method. Next, 100 μL of Spiro-OMeTAD in CB (72.3 $mg{\cdot}mL^{-1}$) containing additives of 17.5 μL of bis(trifluoromethane)-sulfonimide lithium salt (520 $mg{\cdot}mL^{-1}$ in acetonitrile) and 28.8 *μ*L of 4-*tert*-butylpyridine was spin-coated at 4000 rpm for 30 s as a hole transport layer. Finally, 80 nm of Au was deposited as a top electrode using a thermal evaporator system under a vacuum of $\sim 10^{-4}$ Pa.

2. 5 Characterization of perovskite films and devices

The absorption spectra were obtained by using a UV-Vis spectrophotometer (Perkin-Elmer, Lambda 365). X-ray diffraction (XRD) spectra were measured by a Rigaku MiniFlex 600 diffractometer equipped with a Cu*Kα* radiation at room temperature. The ultraviolet photoelectron spectra (UPS) for perovskite films were carried out by using X-ray Photoelectron Spectroscopy (Thermo Fisher, ESCALAB 250Xi). The root-mean-square (RMS) roughness of perovskite films was investigated by Scanning Probe Microscope (Bruker, Dimension Icon). The scanning electron microscopy (SEM) images were obtained by using the Field Emission Scanning Electron Microscope (SU-8010). The *J*-*V* curves were measured by using an Oriel Sol3A simulator (Newport) under AM 1.5 irradiation (100 $mW{\cdot}cm^{-2}$) and recorded by a Keithley 2400 source measurement unit. The light intensity was calibrated by a standard Si reference solar cell that has been certified by the National Renewable Energy Laboratory (NREL). The external quantum efficiency (EQE) measurements were conducted by using a Newport EQE measuring system. The active areas of the devices were fixed at 6.25 mm^2. The unencapsulated 10 devices were tested and stored in the ambient under 65% RH.

3 RESULTS AND DISCUSSION

The DJ phase 2*D* perovskite $(PDA)(MA)_{n-1}Pb_nI_{3n+1}$ (nominal $n = 4$) was prepared from a stoichiometric (4:3:1) reaction between PbI_2, MAI, and $(PDA)I_2$ (see Experimental section for details). In order to identify the difference between 2*D* and 3*D* perovskite films, the $MAPbI_3$ films were

also prepared for comparison. Fig. 2a shows the normalized absorption spectra for the 2*D* and 3*D* perovskite films. The optical bandgap (E_g) can be deduced from the absorption edge according to $E_g = 1240/\lambda$, where λ is the absorption edge. The optical bandgaps of 2*D* and 3*D* perovskite films are 1.67 and 1.60 eV, respectively. X-ray diffraction (XRD) measurements were performed to study the crystallinity of 2*D* and 3*D* perovskite films. As shown in Fig. 2b, both of the perovskite films have two dominant peaks that appear around 14.2 ° and 28.4 °, representing the diffraction from crystallographic planes (111) and (202), respectively[22, 30]. However, the peaks of the 3*D* perovskite film slightly shift towards large angles, which indicates the extension in crystal lattice constant. In the region between 5 ° and 10 °, the 2*D* perovskite film shows the (040) and (060) peaks which characterize the 2*D* perovskites[30]. Ultraviolet photoelectron spectroscopy (UPS) was also conducted to identify the difference between the 2*D* and 3*D* perovskite films on energy levels. The full UPS spectra are given in Fig. 2c. The magnified UPS spectra of the valence band edge (E_{onset}) and the secondary electron cutoff edge (E_{cutoff}) are depicted in Fig. 2d. As shown in Fig. 2d, E_{cutoff} values for the 2*D* and 3*D* perovskite films are 16.10 and 16.22 eV, respectively. Similarly, the 2*D* and 3*D* perovskite films have the same E_{onset} value of 1.77 eV. The highest occupied molecular orbital (HOMO) energy level can be calculated according to HOMO = 21.22 eV − E_{cutoff} + E_{onset}, and the lowest unoccupied molecular orbital (LUMO) energy level can be calculated by the HOMO and optical bandgap[31]. Thus, the HOMO energy levels of 2*D* and 3*D* perovskite films are calculated to be −6.89 and −6.77 eV, respectively, with their corresponding LUMO energy levels to be −5.22 and −5.17 eV, respectively.

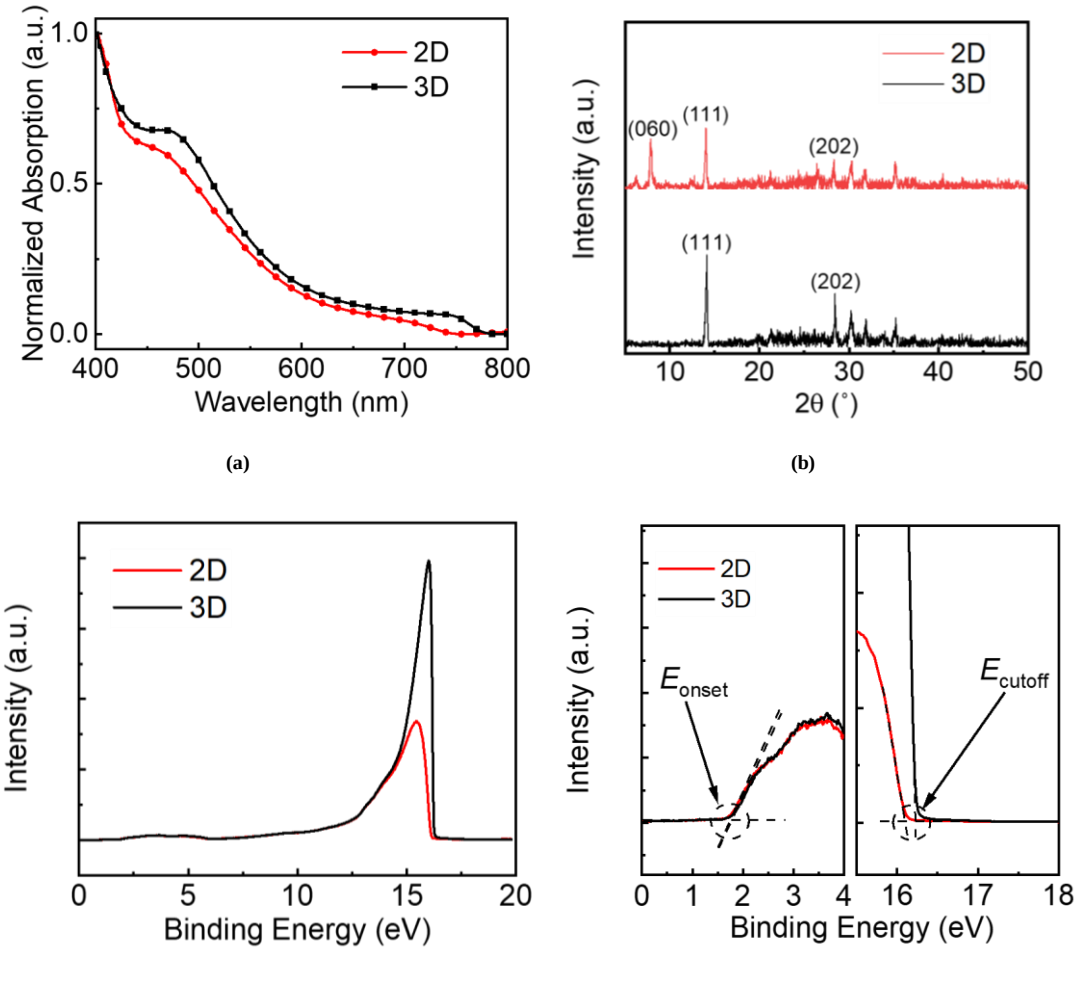

(a) **(b)**

(c) **(d)**

Fig. 2. (a) Absorption spectra of the 2*D* and 3*D* perovskite films. (b) X-ray diffraction (XRD) spectra of the 2*D* and 3*D* perovskite films. (c) Full UPS spectra of the 2*D* and 3*D* perovskite films. (d) UPS spectra for the valence band edge and secondary electron cutoff edge of the 2*D* and 3*D* perovskite films

We also studied the morphological evolution of 2*D* and 3*D* perovskite films by using scanning electron microscopy (SEM) and atomic force microscopy (AFM). The SEM and AFM images of the 2*D* and 3*D* films are shown in Fig. 3. As shown in Fig. 3a, the grain size of 2*D* perovskite is about 50～200 nm, while the 3D perovskite has a larger grain size up to 300 nm (Fig. 3b). The root-mean-square (RMS) roughnesses of the 2*D* and 3*D* films (Fig. 3c and d) are determined to be 4.13 and 7.41 nm, respectively, suggesting the smoother morphology of the 2*D* perovskite film. Besides, the 3*D* perovskite exhibited large grain, which is consistent with the SEM results.

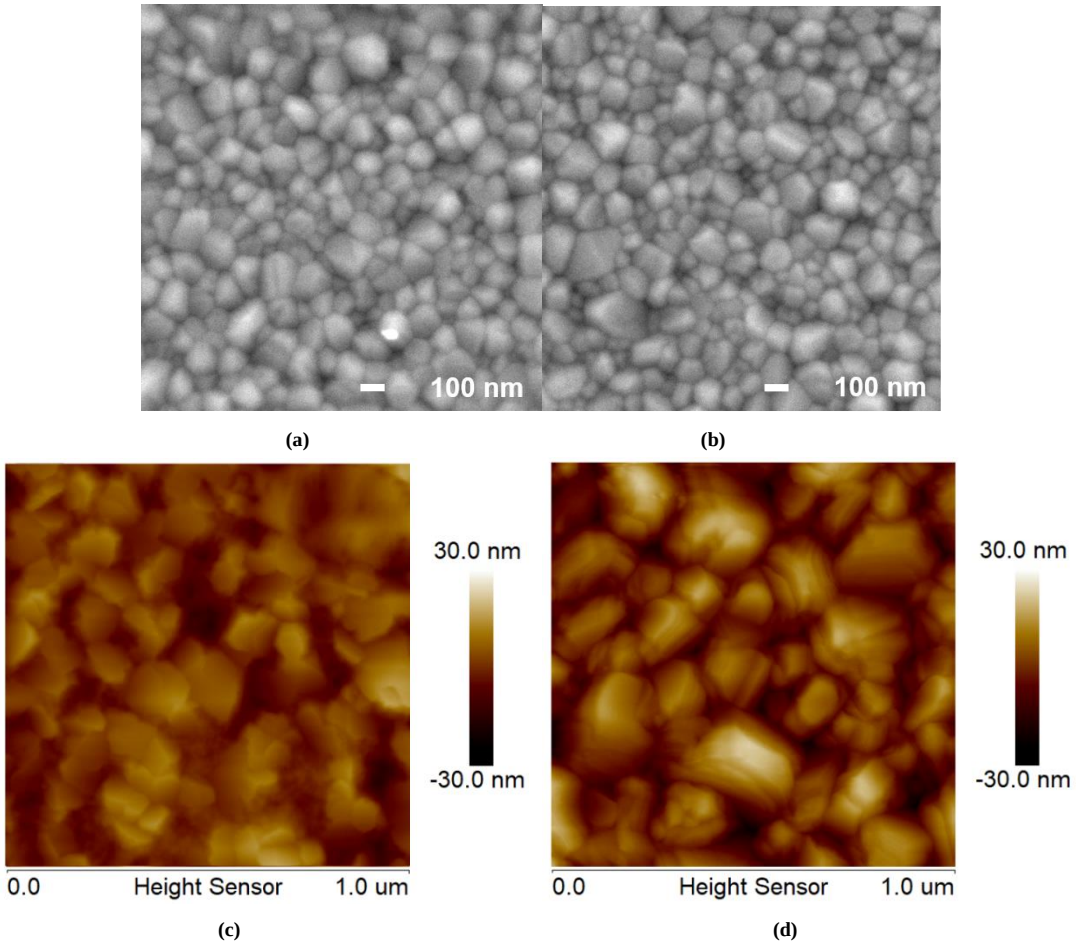

Fig. 3. SEM images of (a) 2*D* and (b) 3*D* perovskite films. The AFM images of (c) 2*D* and (d) 3*D* perovskite films

To investigate the photodetection performance of the (PDA)$(MA)_{n-1}Pb_nI_{3n+1}$ (n = 4) 2*D* perovskite material, photodiodes with a device architecture of ITO/SnO_2/Perovskite/Spiro-OMeTAD/Au (as shown in Fig. 4a and Fig. S1) were fabricated. For comparison purposes, the photodiodes based on 3*D* perovskite were also fabricated with the same device configuration. To prepare the perovskite photodiode, SnO_2 was spin-coated on top of the ITO substrate as an ETL, and then the perovskite film was deposited on the ETL. Later, Spiro-OMeTAD was spin-coated onto the perovskite layer as a hole transport layer (HTL) followed by the sequentially thermal evaporation of Au as a top electrode. To explore the difference between the devices based on 2*D* and 3*D* perovskite films, we tested the external quantum efficiencies (EQEs) of the perovskite photodiodes. The corresponding EQE spectra of the devices are shown in Fig. 4b. The photoresponse range of the devices based on the 2*D* perovskite is 300～750 nm, which is narrower than that of the 3*D* devices (300～800 nm). The trend of EQE spectra is consistent with that of the absorption spectra. The maximum EQE for the devices based on the 3*D* perovskite film is 77% at 470 nm, which is higher than that of the 2*D* devices (67% at 460 nm). The lower EQE for the devices based on 2*D* perovskite film can be attributed to the existence of the insulating PDA layers which hinder the charge transport. As shown in Fig. 4c, the dark current densities of the photodiodes based on 2*D* and 3*D* perovskite films are 9.60×10^{-4} and 3.84×10^{-3} mA·cm^{-2}, respectively. The dark

current of devices based on the 2*D* perovskite film is much lower than that of the 3*D* ones, which is beneficial to improve the on/off ratio of photodiodes. The photocurrent of devices based on the 3*D* perovskite is higher than that of the 2*D* devices (Fig. 4d), which is consistent with the results reported in the literature[28]. The on/off ratio determined by I_{photo}/I_{dark} is 3.10×10^5 for the device based on the 2*D* perovskite film. Owing to its low dark current, the on/off ratio for the 2*D* perovskite-based device is much higher than that of the 3*D* device (7.40×10^3).

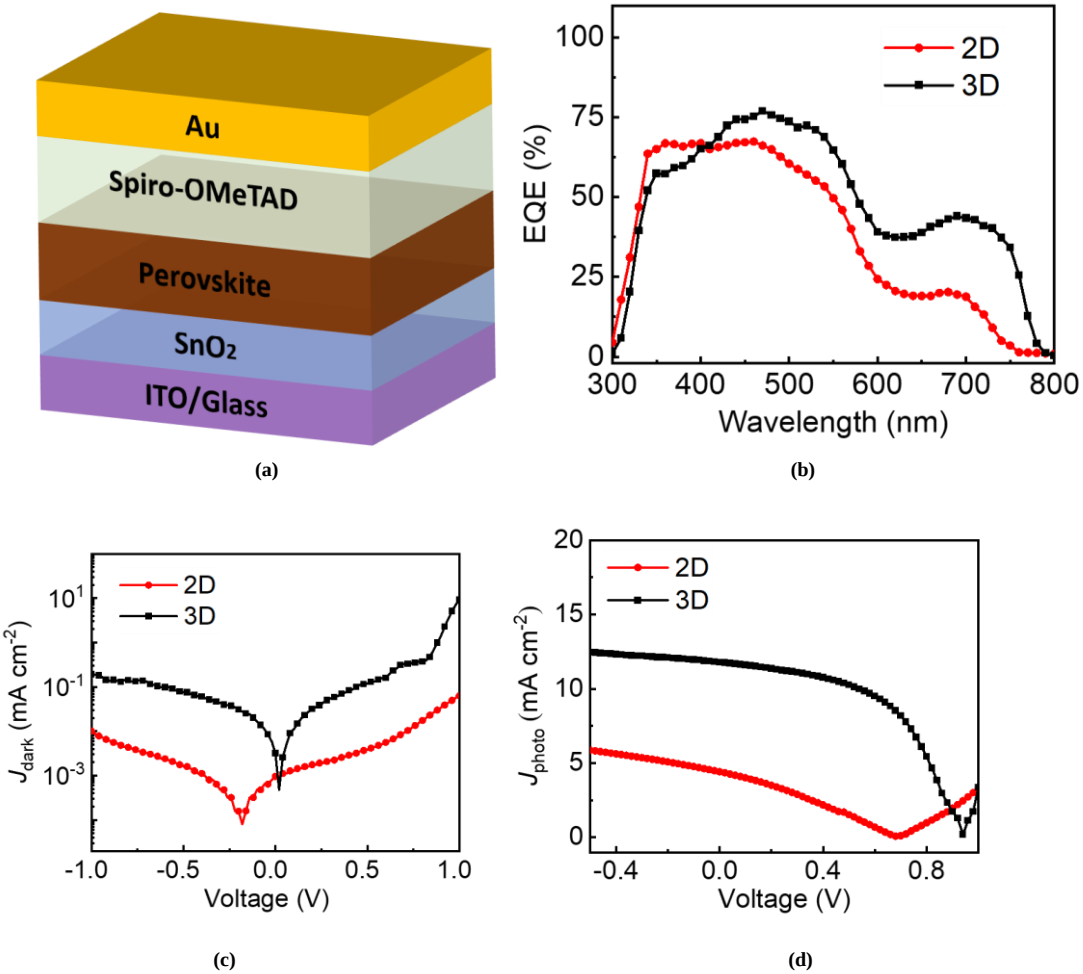

Fig. 4. (a) Configuration of the photodiode. (b) EQE spectra, (c) dark current density, and (d) photocurrent density of the photodiodes based on 2*D* and 3*D* perovskite films measured under one solar (AM 1.5G, 100 mW·cm^{-2}) illumination

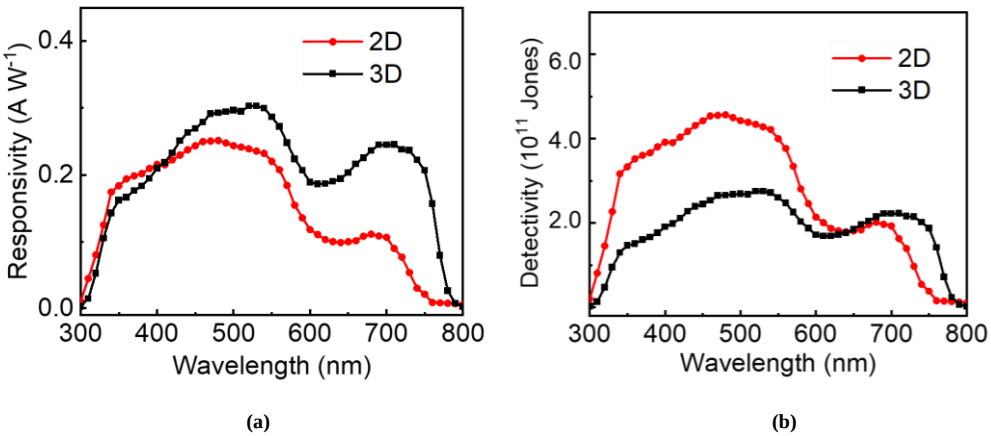

Fig. 5. (a) Responsivity, and (b) detectivity of photodiodes based on the 2*D* and 3*D* perovskite films measured under one solar (AM 1.5G, 100 mW·cm^{-2}) illumination

According to the definition, the responsibility is the ratio of photocurrent to the incident-light intensity, indicating the ability of a device in response to the optical signal. Thereafter, it can be given as follows[16, 32]:

$$R = \frac{J_{\text{photo}}}{L_{\text{light}}} \quad (1)$$

where R is the spectral responsivity, J_{photo} the photocurrent density and L_{light} the incident light intensity. Since EQE can be calculated by the number of photo-generated electrons divided by the number of incident photons, equation (1) can also be described by the following equation (2):

$$R(\lambda) = \frac{EQE \cdot q\lambda}{hc} \quad (2)$$

where q is the electron charge, λ the corresponding wavelength of light, h the Planck's constant, and c the light speed. Using the measured EQE results, we can calculate the wavelength-dependent responsibility of the perovskite photodiodes through equation (2). The highest responsivity data of the perovskite photodiodes were 0.25 $A \cdot W^{-1}$ at 480 nm and 0.30 $A \cdot W^{-1}$ at 530 nm for 2*D* and 3*D* perovskites, respectively (Fig. 5a). The high charge accumulation and increased recombination losses will hinder the photoelectric performance. Thus, the responsivity of the device based on 2*D* perovskite is lower than that of the 3*D* perovskite-based counterpart. Another parameter to evaluate the characteristics of the photodiode is detectivity (*D*). The detectivity characterizes how weak the light can be detected. It is determined by the responsivity and the dark current of a photodetector. In general, the detectivity can be calculated by equation (3):

$$D(\lambda) = \frac{R(\lambda)}{\sqrt{2qJ_{\text{d}}}} \quad (3)$$

where q is the electron charge and J_{d} the dark current density. Considering all of the above equations, a high EQE along with a low dark current can promote the detectivity of a photodetector. The device based on 2*D* perovskite films showed the highest detectivity of 4.57×10^{11} Jones at 480 nm, which is higher than that of 3*D* perovskite-based counterpart (2.76×10^{11} Jones at 530 nm). Although the higher EQE and responsivity were obtained in the devices based on 3*D* perovskite film, the devices based on 2*D* perovskite film exhibited higher detectivity than the 3*D* perovskite-based devices. It can be due to the fact that the organic cation (PDA^+) in the perovskite crystalline structure reduces the dark current. However, the organic cation can also result in the reduction of photocurrent. Therefore, an appropriate amount of organic cations should be used in order to achieve the balance between the photo and dark current. The performance parameters of the devices based on 2*D* and 3*D* perovskite films are summarized in Table 1. Furthermore, we summarized the performance parameters of our and others' work in Table 2. It is shown that the on/off ratio was ultrahigh for the devices based on 2*D* perovskite film in this work, which is 2~3 orders of magnitude higher than the values of the other reported photodetectors based on the DJ phase 2*D* perovskites[28, 29]. Meanwhile, the responsivity and detectivity of 2*D* perovskite-based devices are higher than the reports of DJ-type perovskites.

Table 1. Photodetection Performance Parameters for the Devices Based on 2*D* and 3*D* Perovskite Films

Perovskite	Dark current density ($mA \cdot cm^{-2}$ @ 0V bias)	Responsivity ($A \cdot W^{-1}$ @ 0V bias)	Detectivity (Jones @ 0V bias)	On/off ratio (@ 0V bias)	Maximum on/off ratio
2*D*	9.60×10^{-4}	0.25	4.57×10^{11}	4.60×10^{3}	3.10×10^{5} (@−0.1 V bias)
3*D*	3.84×10^{-3}	0.30	2.76×10^{11}	3.07×10^{3}	7.40×10^{3} (@−0.02 V bias)

Table 2. Comparison of Performance Parameters for the Photodetectors Based on 2*D* DJ Perovskites

Perovskite	Dark current (A)	Responsivity ($mA \cdot W^{-1}$)	Detectivity (Jones)	On/off ratio	Response time	Ref.
$(AMP)(MA)Pb_2I_7$	N/A	0.16 at 532 nm	5.00×10^{10}	6.32×10^{2}	40 ms	[28]
$EDA(MA)_3Pb_4I_{13}$	3.3×10^{-10}	125	7.10×10^{10}	7.50×10^{2}	410/380 μs	[29]
$PDA(MA)_3Pb_4I_{13}$	6.0×10^{-8}	250 at 480 nm	4.56×10^{11}	3.10×10^{5}	20/45 ms	This work

As can be seen from Table 1, the photodiodes based on 2*D* perovskite displayed better performance with a lower dark current, higher detectivity and on/off ratio. Since stability is the most prominent advantage of 2*D* perovskite materials compared to 3*D* ones, the stability of both unencapsulated devices was investigated under ambient condition (65% RH). The normalized photocurrent densities and the dark current densities of two types of photodiodes as a function of time are shown in Fig. 6. As shown in Fig. 6a, the normalized photocurrent density of the 3*D* perovskite-photodiode showed a great decrease and only maintained 35% of the initial photocurrent value after 90 days of storage. In contrast, the 2*D* perovskite-photodiode exhibited significantly improved stability with 95% of the initial photocurrent under the same storage condition. Fig. 6b shows the dark current densities of the two types of devices as a function of time. The dark current density of the devices based on 2*D* perovskites maintained ~10^{-4} mA·cm^{-2} all along, while that of the 3*D* ones increased from 3.84 × 10^{-3} mA·cm^{-2} to 5.80 × 10^{-3} mA·cm^{-2} after 90 days. It is well known that the increase of dark current is detrimental to the device performance. Therefore, the devices based on 2*D* perovskites are more promising in practical applications.

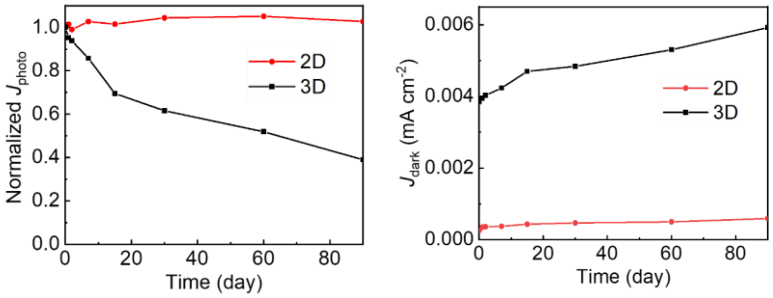

(a) (b)

Fig. 6. (a) Normalized photocurrent density, (b) the dark current density of the photodiodes based on 2*D* and 3*D* perovskite films as a function of the storage time

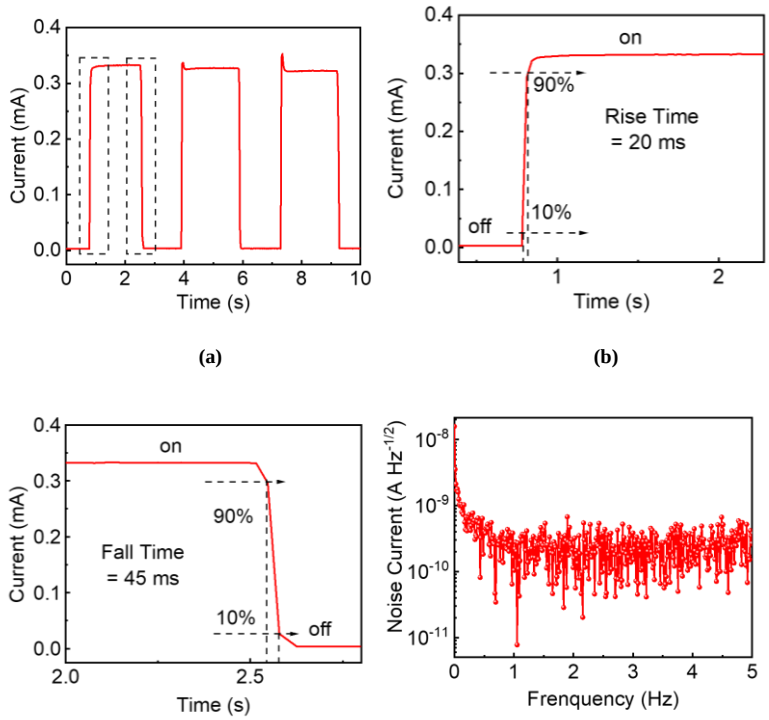

(a) (b)

(c) (d)

Fig. 7. Photoresponse performance of photodiodes based on 2*D* perovskite film measured under the repeated cycles of illumination of one solar light (100 mW·cm^{-2}, AM 1.5G). (a) Time-dependent photocurrent response (*I*-*t*) curves. (b) Rise time. (c) Fall time. (d) The noise current measured under one solar (100 mW·cm^{-2}, AM 1.5 G) illumination

We further investigated the light response speed of the photodiode based on 2*D* perovskite film by testing the response time of the device under one solar light illumination (Figs. 7a and S2). Fig. 7a shows the time-dependent photocurrent response curves within 10 s under switching state. Fig. 7b and c show the rise and fall time of the photodiode, respectively. The rise time (fall time) is defined as the time for the photocurrent to rise from 10% to 90% (fall from 90% to 10%) of the maximum value during the on and off cycles[31, 33, 34]. The calculated rise time for the 2*D* perovskite-based photodiode is 20 ms and the fall time is 45 ms, which exhibited comparable response time with the devices reported by others[25, 28]. The fast rise and fall time suggested the fast response speed of the devices based on 2*D* perovskite. Fig. 7d shows the level of the noise current of the 2*D* perovskite-based photodiode. It is found that the overall noise current is stable at 10^{-9}～10^{-10} A·Hz$^{-1/2}$. Moreover, the noise current stabilized quickly at low frequencies (within 5 Hz), which is also of great significance for the practical application of the photodiodes. The highest on/off ratio of the device based on 2*D* perovskite is 3.10×10^5, which is impressive for 2*D* perovskite-based photodiodes. The unencapsulated photodiodes based on 2*D* perovskite can be stored under air with RH of 65% for over 90 days without significant degradation, showing their improved stability than the 3*D* perovskite-based photodiodes. This long-term stable 2*D* Dion-Jacobson phase perovskite photodiode with low dark current and high on/off ratio is promising for the practical switching applications.

4 CONCLUSION

In summary, we incorporated a diamine (PDA) into the conventional 3*D* perovskite component to form a DJ phase 2*D* perovskite PDA$(MA)_{n-1}Pb_nI_{3n+1}$ (nominal n = 4). The photodiode based on 2*D* perovskite exhibited better performance with a high detectivity (4.57×10^{11} Jones at 480 nm) and a low dark current density (9.60×10^{-4} mA·cm^{-2}) in comparison with the device based on 3*D* perovskite. Also,

REFERENCES

(1) Konstantatos, G.; Sargent, E. H. Nanostructured materials for photon detection. *Nat. Nanotechnol*. **2010**, 5, 391–400.

(2) Xue, J.; Zhu, Z.; Xu, X.; Gu, Y.; Wang, S.; Xu, L.; Zou, Y.; Song, J.; Zeng, H.; Chen, Q. Narrowband perovskite photodetector-based image array for potential application in artificial vision. *Nano Lett.* **2018**, 18, 7628–7634.

(3) Cen, G.; Liu, Y.; Zhao, C.; Wang, G.; Fu, Y.; Yan, G.; Yuan, Y.; Su, C.; Zhao, Z.; Mai, W. Atomic-layer deposition-assisted double-side interfacial engineering for high-performance flexible and stable $CsPbBr_3$ perovskite photodetectors toward visible light communication applications. *Small* **2019**, 15, 1902135–9.

(4) Zhang, Z. X.; Li, C.; Lu, Y.; Tong, X. W.; Liang, F. X.; Zhao, X. Y.; Wu, D.; Xie, C.; Luo, L. B. Sensitive deep ultraviolet photodetector and image sensor composed of inorganic lead-free $Cs_3Cu_2I_5$ perovskite with wide bandgap. *J. Phys. Chem. Lett.* **2019**, 10, 5343–5350.

(5) Shan, G.; Li, X.; Huang, W. AI-enabled wearable and flexible electronics for assessing full personal exposures. *The Innovation* **2020**, 1, 100031–2.

(6) Jalali, B.; Fathpour, S. Silicon photonics. *J. Lightwave Technol*. **2006**, 24, 4600–4615.

(7) Michel, J.; Liu, J.; Kimerling, L. C. High-performance Ge-on-Si photodetectors. *Nat. Photonics* **2010**, 4, 527–534.

(8) Kang, K.; Xie, S.; Huang, L.; Han, Y.; Huang, P. Y.; Mak, K. F.; Kim, C. J.; Muller, D.; Park, J. High-mobility three-atom-thick semiconducting films with wafer-scale homogeneity. *Nature* **2015**, 520, 656–660.

(9) Xu, K.; Xiao, X.; Zhou, W.; Jiang, X.; Wei, Q.; Chen, H.; Deng, Z.; Huang, J.; Chen, B.; Ning, Z. Inverted Si:PbS colloidal quantum dot heterojunction-based infrared photodetector. *ACS Appl. Mater. Interfaces* **2020**, 12, 15414–15421.

(10) Liu, N.; Huang, C. Y.; Zhu, L.; Chen, Y.; Xu, G. W.; Chu, L.; Ma, X. G. Organic cation effect on the physical properties of $CH_3NH_3PbI_3$ perovskite from the first-principles study. *Chin. J. Struct. Chem.* **2016**, 35, 1297–1305.

(11) Jeon, N. J.; Noh, J. H.; Yang, W. S.; Kim, Y. C.; Ryu, S.; Seo, J.; Seok, S. I. Compositional engineering of perovskite materials for high-performance solar cells. *Nature* **2015**, 517, 476–480.

(12) Noh, J. H.; Im, S. H.; Heo, J. H.; Mandal, T. N.; Seok, S. I. Chemical management for colorful, efficient, and stable inorganic-organic hybrid nanostructured solar cells. *Nano Lett.* **2013**, 13, 1764–1769.

(13) Dong, Q.; Fang, Y.; Shao, Y.; Mulligan, P.; Qiu, J.; Cao, L.; Huang, J. Electron-hole diffusion lengths > 175 μm in solution-grown $CH_3NH_3PbI_3$ single crystals. *Science* **2015**, 347, 967–970.

(14) Tan, Z. K.; Moghaddam, R. S.; Lai, M. L.; Docampo, P.; Higler, R.; Deschler, F.; Price, M.; Sadhanala, A.; Pazos, L. M.; Credgington, D.; Hanusch,

F.; Bein, T.; Snaith, H. J.; Friend, R. H. Bright light-emitting diodes based on organometal halide perovskite. *Nat. Nanotechnol.* **2014**, 9, 687–692.

(15) Baikie, T.; Fang, Y.; Kadro, J. M.; Schreyer, M.; Wei, F.; Mhaisalkar, S. G.; Graetzel, M.; White, T. J. Synthesis and crystal chemistry of the hybrid perovskite (CH_3NH_3) PbI_3 for solid-state sensitised solar cell applications. *J. Mater. Chem. A* **2013**, 1, 5628–5641.

(16) Dou, L.; Yang, Y.; You, J.; Hong, Z.; Chang, W. H.; Li, G.; Yang, Y. Solution-processed hybrid perovskite photodetectors with high detectivity. *Nat. Comnun.* **2014**, 5, 5404–6.

(17) Stranks, S. D.; Snaith, H. J. Metal-halide perovskites for photovoltaic and light-emitting devices. *Nat. Nanotechnol.* **2015**, 10, 391–402.

(18) Tan, H.; Jain, A.; Voznyy, O.; Lan, X.; Garc á de Arquer, F. P.; Fan, J. Z.; Quintero-Bermudez, R.; Yuan, M.; Zhang, B.; Zhao, Y.; Fan, F.; Li, P.; Quan, L. N.; Zhao, Y.; Lu, Z. H.; Yang, Z.; Hoogland, S.; Sargent, E. H. Efficient and stable solution-processed planar perovskite solar cells via contact passivation. *Science* **2017**, 355, 722–5.

(19) Ahmad, S.; Fu, P.; Yu, S.; Yang, Q.; Liu, X.; Wang, X.; Wang, X.; Guo, X.; Li, C. Dion-Jacobson phase 2*D* layered perovskites for solar cells with ultrahigh stability. *Joule* **2019**, 3, 794–806.

(20) Chen, H.; Xia, Y.; Wu, B.; Liu, F.; Niu, T.; Chao, L.; Xing, G.; Sum, T.; Chen, Y.; Huang, W. Critical role of chloride in organic ammonium spacer on the performance of Low-dimensional Ruddlesden-Popper perovskite solar cells. *Nano Energy* **2019**, 56, 373–381.

(21) Smith, I. C.; Hoke, E. T.; Solis-Ibarra, D.; McGehee, M. D.; Karunadasa, H. I. A layered hybrid perovskite solar-cell absorber with enhanced moisture stability. *Angew. Chem. Int. Ed.* **2014**, 53, 11232–11235.

(22) Tsai, H.; Nie, W.; Blancon, J. C.; Stoumpos, C. C.; Asadpour, R.; Harutyunyan, B.; Neukirch, A. J.; Verduzco, R.; Crochet, J. J.; Tretiak, S.; Pedesseau, L.; Even, J.; Alam, M. A.; Gupta, G.; Lou, J.; Ajayan, P. M.; Bedzyk, M. J.; Kanatzidis, M. G.; Mohite, A. D. High-efficiency two-dimensional Ruddlesden-Popper perovskite solar cells. *Nature* **2016**, 536, 312–316.

(23) Han, S.; Yao, Y.; Liu, X.; Li, B.; Ji, C.; Sun, Z.; Hong, M.; Luo, J. Highly oriented thin films of 2*D* Ruddlesden-Popper hybrid perovskite toward superfast response photodetectors. *Small* **2019**, 15, 1901194–6.

(24) Tsai, H.; Liu, F.; Shrestha, S.; Fernando, K.; Tretiak, S.; Scott, B.; Vo, D. T.; Strzalka, J.; Nie, W. A sensitive and robust thin-film X-ray detector using 2*D* layered perovskite diodes. *Sci. Adv.* **2020**, 6, eaay0815–7.

(25) Lim, J. W.; Wang, H.; Choi, C. H.; Kwon, H.; Quan, L. N.; Park, W. T.; Noh, Y. Y.; Kim, D. H. Self-powered reduced-dimensionality perovskite photodiodes with controlled crystalline phase and improved stability. *Nano Energy* **2019**, 57, 761–770.

(26) Niu, T.; Ren, H.; Wu, B.; Xia, Y.; Xie, X.; Yang, Y.; Gao, X.; Chen, Y.; Huang, W. Reduced-dimensional perovskite enabled by organic diamine for efficient photovoltaics. *J. Phys. Chem. Lett.* **2019**, 10, 2349–2356.

(27) Lu, D.; Lv, G.; Xu, Z.; Dong, Y.; Ji, X.; Liu, Y. Thiophene-based two-dimensional Dion-Jacobson perovskite solar cells with over 15% efficiency. *J. Am. Chem. Soc.* **2020**, 142, 11114–11122.

(28) Park, I. H.; Kwon, K. C.; Zhu, Z.; Wu, X.; Li, R.; Xu, Q. H.; Loh, K. P. Self-powered photodetector using two-dimensional ferroelectric Dion-Jacobson hybrid perovskites. *J. Am. Chem. Soc.* **2020**, 142, 18592–18598.

(29) Lai, Z.; Dong, R.; Zhu, Q.; Meng, Y.; Wang, F.; Li, F.; Bu, X.; Kang, X.; Zhang, H.; Quan, Q.; Wang, W.; Wang, F.; Yip, S.; Ho, J. C. Bication-mediated quasi-2*D* halide perovskites for high-performance flexible photodetectors: from Ruddlesden-Popper type to Dion-Jacobson type. *ACS Appl. Mater. Interfaces* **2020**, 12, 39567–39577.

(30) Cao, D. H.; Stoumpos, C. C.; Farha, O. K.; Hupp, J. T.; Kanatzidis, M. G. 2*D* homologous perovskites as light-absorbing materials for solar cell applications. *J. Am. Chem. Soc.* **2015**, 137, 7843–7850.

(31) Cao, F.; Tian, W.; Deng, K.; Wang, M.; Li, L. Self-powered UV-Vis-NIR photodetector based on conjugated-polymer/$CsPbBr_3$ nanowire array. *Adv. Funct. Mater.* **2019**, 29, 1906756–7.

(32) Ahmadi, M.; Wu, T.; Hu, B. A review on organic-inorganic halide perovskite photodetectors: device engineering and fundamental physics. *Adv. Mater.* **2017**, 29, 1605242–24.

(33) Bansode, U.; Rahman, A.; Ogale, S. Low-temperature processing of optimally polymer-wrapped α-$CsPbI_3$ for self-powered flexible photo-detector application. *J. Mater. Chem. C* **2019**, 7, 6986–6996.

(34) Wang, K.; Wu, C.; Yang, D.; Jiang, Y.; Priya, S. Quasi-two-dimensional halide perovskite single crystal photodetector. *ACS Nano* **2018**, 12, 4919–4929.